

The Birmingham–CfA cluster scaling project – II. Mass composition and distribution

A. J. R. Sanderson^{1,2★} and T. J. Ponman¹

¹*School of Physics and Astronomy, University of Birmingham, Edgbaston, Birmingham B15 2TT*

²*Department of Astronomy, University of Illinois, 1002 West Green Street, Urbana, IL 61801, USA*

Accepted 2003 July 23. Received 2003 July 22; in original form 2003 March 11

ABSTRACT

We investigate the spatial distribution of the baryonic and non-baryonic mass components in a sample of 66 virialized systems. We have used X-ray measurements to determine the deprojected temperature and density structure of the intergalactic medium and have employed these to map the underlying gravitational potential. In addition, we have measured the deprojected spatial distribution of galaxy luminosity for a subset of this sample, spanning over two decades in mass. With this combined X-ray/optical study, we examine the scaling properties of the baryons and address the issue of mass-to-light (M/L) ratio in groups and clusters of galaxies.

We measure a median mass-to-light ratio of $249 h_{70}(M/L)_{\odot}$ in the rest frame B_J band, in good agreement with other measurements based on X-ray determined masses. There is no trend in M/L with X-ray temperature and no significant trend for mass to increase faster than luminosity: $M \propto L_{B_J}^{1.08 \pm 0.12}$. This implied lack of significant variation in star formation efficiency suggests that gas cooling cannot be greatly enhanced in groups, unless it drops out to form baryonic dark matter. Correspondingly, our results indicate that non-gravitational heating must have played a significant role in establishing the observed departure from self-similarity in low-mass systems. The median baryon fraction for our sample is $0.162 h_{70}^{-3/2}$, which allows us to place an upper limit on the cosmological matter density, $\Omega_m \leq 0.27 h_{70}^{-1}$, in good agreement with the latest results from *WMAP*.

We find evidence of a systematic trend towards higher central density concentration in the coolest haloes, indicative of an early formation epoch and consistent with hierarchical formation models.

Key words: galaxies: clusters: general – intergalactic medium – X-rays: galaxies: clusters.

1 INTRODUCTION

As the material most amenable to detailed study, the properties of optically luminous matter have long been used to infer the distribution of mass in the Universe. Clusters of galaxies provide an excellent laboratory for this purpose, since they are sufficiently large that their global properties reflect those of the Universe as a whole.

Previous work has shown that both optical light and gas, in particular, are more spatially extended than the dark matter within virialized systems (David, Jones & Forman 1995). Evidence of a monotonic rise in gas fraction with radius has also been found across a wide range of mass scales in a very large sample of virialized systems (Sanderson et al. 2003, hereafter Paper I), and also in the recent analysis of Castillo-Morales & Schindler (2003), which is in broad agreement with numerical simulations (Eke, Navarro & Frenk 1998; Frenk et al. 1999). This behaviour has been further confirmed in a

high-quality *XMM–Newton* observation of a relaxed cluster (Pratt & Arnaud 2002), where the X-ray halo has been traced out almost to the virial radius, although *Chandra* observations of extremely relaxed lensing clusters have revealed a flat gas fraction profile in a small number of cases (Allen, Schmidt & Fabian 2002). However, the latter observations only probe approximately the innermost one-third of the halo: our data, though of poorer quality, extend beyond this region in many cases, and we benefit from averaging over a large ensemble of virialized systems.

While the hot gas has been shown to depart systematically from self-similarity under the influence of non-gravitational physics, the same cannot be said of the dark matter, which is not directly affected by such processes. N -body simulations indicate that the dark matter of virialized haloes should follow a universal profile, across a wide range of scale sizes (Navarro, Frenk & White 1995), apart from a mild trend in its concentration with mass (Navarro, Frenk & White 1997; Salvador-Solé, Solanes & Manrique 1998; Avila-Reese et al. 1999; Jing 2000).

★E-mail: ajrs@astro.uiuc.edu

Although the contribution to the baryonic mass component from the individual galaxies in virialized systems is significantly less than that from the X-ray emitting intergalactic medium, the galaxy component is of great importance, none the less. As the ultimate end-point of gas cooling, as well as the source of non-gravitational energy injection into the intergalactic medium (IGM), the behaviour of the stars is closely linked to the properties of the gas. In addition, stellar sources are responsible for the synthesis of the metals that contaminate the IGM, which are released via supernova-driven winds (e.g. Finoguenov, Arnaud & David 2001a).

However, the scaling properties of the stellar content are rather less well established than those of the IGM. In particular, there is some debate on the mass-to-light ratio in groups and clusters and how this compares with the global value. Recent studies have reached differing conclusions about how this quantity scales with halo mass. For example, Girardi et al. (2002) report a trend towards increased M/L in clusters, a result also favoured by Marinoni & Hudson (2002). By contrast, measurements of M/L based on X-ray mass estimates have concluded that it is roughly universal in groups and clusters (Cirimele, Nesci & Trévese 1997; Hradecky et al. 2000).

The approach of a combined X-ray and optical analysis of clusters and groups of galaxies is a powerful tool for the understanding of mass distribution in these systems. The X-ray data yield information about the behaviour of the diffuse, hot IGM, and can be used to determine the underlying gravitational potential structure, under the assumption of hydrostatic equilibrium. By contrast, optical measurements can be used to map the spatial properties of the baryons resident in luminous matter, and hence deduce their contribution to the total mass budget.

In Paper I, we presented a detailed X-ray analysis of the IGM in a large sample of 66 virialized systems, allowing us to reconstruct the properties of the IGM. We have assembled our sample from three existing X-ray studies of groups and clusters, to which we have added a small number of cool groups. To each system, we have fitted analytical profiles to parametrize both the gas density and temperature as a function of radius. This allows us to place all the X-ray data on a unified footing, giving us the freedom to extrapolate the gas properties to arbitrary radius. As with detailed X-ray analyses, previous combined X-ray/optical studies of this nature have been restricted to relatively small sample sizes (e.g. Cirimele et al. 1997; Hradecky et al. 2000). In this paper, we build on our modelling of the IGM, by incorporating the spatial distribution of stellar material, which also allows us to determine the distribution of dark matter. Despite only covering half our original sample (some 32 groups and clusters), our optical sample is well suited to the study of the scaling properties of these systems, since we retain good coverage across a wide range of system masses.

Throughout this paper we adopt the following cosmological parameters: $H_0 = 70 \text{ km s}^{-1} \text{ Mpc}^{-1}$ and $q_0 = 0$. All quoted errors are 1σ on one parameter, unless otherwise stated.

2 THE 3D GALAXY DENSITY CALCULATION

The task of mapping the stellar mass in virialized systems is complicated by the discrete nature of the individual galaxies – unlike the evenly distributed gas, which smoothly traces the underlying gravitational potential. In addition, the contrast against the background of a cluster or group of galaxies is much lower at optical wavelengths, scaling only linearly with number density, rather than in proportion to ρ_{gas}^2 in the case of X-ray emission. These two difficulties

are further compounded by the large angular size subtended by a typical group or cluster, which may exceed one degree on the sky – significantly larger than can be viewed by many current-generation wide-field charge-coupled device (CCD) cameras. Correspondingly, there have been comparatively few detailed photometric studies of rich clusters made with CCDs (e.g. Carlberg, Yee & Ellingson 1997).

One way to avoid some of the above problems is to establish cluster membership quantitatively with redshift measurements of individual galaxies in its vicinity. Although this avoids the need to estimate the background contribution, such an advantage comes only at the price of long observing times, in order to obtain high-quality spectra for a large fraction of the galaxy members. For this reason such studies are restricted to a small number of clusters (e.g. Fabricant, Kent & Kurtz 1989; Girardi et al. 1995; Mohr et al. 1996; Koranyi & Geller 2000, 2002). Given these limitations, we have taken a different approach to the issue of measuring the spatial distribution of galaxies and then estimating the total luminosity of the whole system. We outline below our method, which is based on widely available digitized photographic plate data derived from all-sky surveys.

The process can be separated into two stages: first, determination of the spatial distribution of the galaxy number density (see Section 2.3); and, secondly, the calculation of the normalization of this density profile (see Section 3.2). Although the normalization can, of course, be calculated in the spatial fitting, this makes no allowance for the contribution to the total luminosity from galaxies too faint to be observed. To estimate this contribution, it is necessary to determine the luminosity function of the observed galaxies and to extrapolate this down to some limiting magnitude, in order to correct for the missing light. Whilst it is possible to do this using photographic plate-based data, the measured magnitudes require careful calibration, as a result of subtle variations in the sensitivity of the photographic emulsion both within and between plates. Therefore, we have taken integrated luminosity values from a small number of sources in the literature and used these to infer a three-dimensional normalization, in combination with our fitted profile parameters.

We assume a distribution of optical light described by an NFW profile (Navarro et al. 1995), i.e.

$$\rho = \frac{\rho_0}{x(1+x)^2}, \quad (1)$$

where $x = r/r_s$ and r_s is a characteristic scale radius. This function rises from a logarithmic slope of -3 at large radii to a central cusp ($\rho \propto r^{-1}$), with the transition between the two regimes occurring around r_s . Such a parametrization is advantageous as it has only one free parameter (since the normalization is constrained by our maximum-likelihood fitting method – see Section 2.3), which helps to stabilize the fitting, given the relatively large background level in the case of the plate data.

We make the assumption of spherical symmetry in the deprojection of the optical light distribution, as we did for the X-ray analysis in Paper I. Since our sample has been selected on the basis of a relaxed X-ray morphology, it is reasonable to expect a corresponding degree of regularity in the galaxy distribution. This also improves the quality of the fit, which might otherwise be degraded by the presence of significant substructure or bimodality. However, despite this, it was not possible to obtain a satisfactory surface density fit to the photographic plate data for a small number of cool groups; their treatment is described in Section 2.2 below.

2.1 Automatic Plate Measuring data

The Automatic Plate Measuring (APM) machine source catalogue¹ is a digitized catalogue based on the first-generation Palomar Observatory Sky Survey (POSS I) and United Kingdom Schmidt Telescope (UKST) photographic plates. The field of view covered is extremely large – 6.2 and 5.8 degrees on a side for the plates from POSS I and UKST, respectively – and the whole sky has been observed in this way. As such, it is ideal for studying large-scale structure at optical wavelengths, although the magnitude information it provides can be rather unreliable, owing to saturation and other problems with photographic emulsions. However, we only exploit the positional data available – which are very reliable – since we determine total luminosities for our groups and clusters from literature measurements.

To extract source positions for our fitting, we have applied very conservative selection criteria to allow for problems with source identification. Although detection algorithms have been used to distinguish between stellar and non-stellar sources, this classification is often unreliable and can cause stars to be identified as galaxies (e.g. Caretta, Maia & Willmer 2000) and vice versa: in a recent analysis of data from the Minnesota Automated Plate Scanner (APS) digitized survey of POSS I plates, Rines et al. (2002) found that ~ 3.3 per cent of objects identified as stars were actually galaxies, in the vicinity of the cluster Abell 2199. This confusion is exacerbated for faint galaxies, and consequently we only neglect sources classified as stars if they are brighter than $m_b = 15$; otherwise all detected sources are used. This avoids any potential systematic bias in the fitting between clusters, at the expense of a significantly increased background level. All objects classified as noise features are excluded.

2.2 NASA/IPAC Extragalactic Database data

The problems associated with optical analysis are exacerbated at the scale of groups of galaxies, which present even lower contrast against the background, owing to their smaller volume. However, many well-studied groups – including most of those in our sample – are sufficiently close so as to have measured recession velocities available in the literature. In such cases it is therefore possible to establish unambiguous membership of the group, thus eliminating the contamination from fore- and background objects. However, the numbers of such confirmed members are generally rather small and tend to be predominantly limited to the inner regions of the halo. The impact of this is mitigated to some extent by our chosen parametrization of galaxy density (equation 1), which has only a single free parameter (the scale radius, r_s), since sparse data obviously provide weaker constraints on spatial fitting (e.g. Girardi et al. 1995).

It was not possible to derive NFW scale radii from the APM data for four of our groups (NGC 2563, 5129, 5846 and 6338) and so we took galaxy positions from the NASA/IPAC Extragalactic Database (NED) for these systems. We used only those galaxies which were identified as being group members in the data base. It was also necessary to do this for Abell 539, since no POSS I or UKST data were available for this poor cluster. There is potential for bias when using NED data, since the completeness properties of the data base are unknown – although we are only concerned with the spatial completeness, since the luminosities for these systems are taken from

other sources. In particular, it is possible that there may be a dearth of galaxies catalogued in the outer regions of these groups, which may introduce a spurious central surface density enhancement. However, we note that any such bias is reduced by the fact that we have used the radius of the outermost galaxy as the cut-off radius in the fitting, rather than the X-ray determined virial radius used to select the galaxies from NED.

2.3 Surface density fitting

As we are interested in the three-dimensional properties of the galaxy optical light, we have chosen to parametrize the space density distribution in three dimensions and then numerically project this, for comparison with the surface density of galaxies. The same approach was used in the deprojection of the X-ray data (see Paper I). This method is advantageous, since it directly yields the required parameters, without the need for inversion. For the analysis of the APM data, a constant background term was included as a free parameter, to allow for a variation in the number of fore- or background sources caused, for example, by differences in large-scale structure along the line of sight. It is important to fit this separately for each cluster, since our background (incorporating a stellar component) can vary significantly with position on the sky. The centroid of the model was fixed at the cluster position as listed in NED, in order to stabilize the fitting. Although the optical centroid can be displaced with respect to the X-ray centroid, we note that Girardi et al. (2000) find a typical error in L_B within R_v of just 5 per cent, when recomputing their integrated optical luminosities using an X-ray rather than optical centroid.

The three-dimensional density profile was evaluated in a series of spherical shells, by numerically integrating equation (1) between their radial boundaries. For each spherical shell there is a corresponding annulus, with identical radial bounds. The surface density in each annulus is calculated by summing the contributions made to it by its corresponding shell and all those lying outside it. Hence the contribution to the surface density from projection along the line of sight is fully accounted for.

We have chosen to perform an *unweighted* fit to the data (as also used by Hradecky et al. 2000 and Koranyi & Geller 2002, for example), so that each galaxy is treated as a single point at a given position. This approach is advantageous since it avoids the need to use plate-measured magnitudes, which require careful calibration as mentioned above. By treating each galaxy identically we are implicitly assuming that there is no luminosity segregation, i.e. that the luminosity function is everywhere the same within the cluster. This is a reasonable assumption, since any segregation is generally limited to only the very brightest galaxies – which tend to be located more centrally in clusters (Adami, Katgert & Biviano 1998).

The use of an unweighted fit has important consequences for those clusters that possess a central cD galaxy. On the one hand, our method limits the potential for an extremely bright, centrally located galaxy to skew the fit, by overemphasizing the central luminosity density. On the other hand, in so doing, there is a tendency to slightly overestimate the luminosity in the outer regions. This is due to our method for determining the luminosity normalization, which does include a contribution from any central cD object. As a result, the extra luminosity of such a galaxy is, in effect, ‘spread out’ over the whole profile, leading to an artificial excess in the outer regions. However, the effect of this on our total luminosity estimates is small, given the generally large sizes of the apertures used to measure the luminosity values to which we normalize our density profiles (see Section 3.2). In any case, the contribution to the luminosity function

¹ <http://www.ast.cam.ac.uk/~apmcat/>

from cD galaxies is fully accounted for by this same method for determining the total cluster luminosity.

Although some previous studies of galaxy distributions in clusters have fitted analytical profiles with cores to the data (e.g. Girardi et al. 1995; Cirimele et al. 1997), we favour the cusped NFW profile (equation 1). Not only does it have one fewer fitted parameter – which helps to stabilize the fitting, as previously mentioned – but also it provides a more accurate description of the dark matter distribution (Navarro et al. 1995). Simulations indicate that the galaxies trace the dark matter more closely than the gas does, with only a modest bias (Davé, Katz & Weinberg 2002); they may even be more centrally concentrated, owing to the effects of dynamical friction (Metzler & Evrard 1997). We note that Adami et al. (1998) have shown that only the surface density of faint galaxies shows a significant preference for a distribution with a core rather than a cusp. Since our analysis is based on photographic plate observations, rather than the higher-quality CCD data used in their work, we can therefore expect to be relatively insensitive to this effect.

Previous studies offer support for the presence of a cusp in the luminosity distribution. For example, Oegerle, Jewison & Hoessel (1987) measure a power-law slope of approximately -1 in the centres of three Abell clusters; Merritt & Tremblay (1994) find evidence of a central power-law dependence of galaxy space density in the core of the Coma cluster, using a non-parametric algorithm. Beers & Tonry (1986) have demonstrated that imperfect centring can ‘erase’ the presence of a real cusp and artificially introduce a constant density core. Using two methods of determining the cluster centre, they find that the majority of the 48 clusters in their sample possess a central cusp in projected galaxy density. The inner regions of these clusters are well characterized by a power-law slope of -1 .

We use the maximum-likelihood fitting procedure described in Sarazin (1980), which we now briefly outline. There are three parameters to be determined – the scale radius r_s , the surface density normalization Σ_0 , and background surface density Σ_{bg} (since the centroid is fixed – see above). However, only two of these parameters are independent, and therefore we require an additional constraint, otherwise the maximum-likelihood solution is unbounded. We apply the condition that the model reproduces the observed number of galaxies within the fitting region. In the standard method of Sarazin (1980), r_s and Σ_0 are left as free parameters and Σ_{bg} is calculated so that the ‘area’ under the model plus background equals the total number of galaxies within the fitting region. However, in the case of our NED data, Σ_{bg} is known *a priori* (i.e. it is zero, since all the galaxies are confirmed group members), so we use the alternative method detailed in section IV of Sarazin (1980). Here, Σ_{bg} and r_s are left as fitted parameters, while Σ_0 is instead calculated so as to reproduce the observed galaxy count.

As a result of our numerical projection technique, Σ_0 is not actually a direct model parameter. However, it is trivially related to ρ_0 , the NFW central density normalization from equation (1). We determine the appropriate value of ρ_0 by setting it initially to unity and calculating the ‘area’ under the projected data, excluding the parts of any annuli lying outside the fit region, i.e. summing the product of the surface density in each annulus and its area. The ratio of the observed number of galaxies in the fitting region to this number then yields ρ_0 .

Fitting was performed using the gradient-based MIGRAD method in the MINUIT minimization library from CERN (James 1998), and errors on the parameters were found with MINOS, from the same package. Errors were determined from the increase in the Cash statistic of one, since differences between values obtained from the same data set are χ^2 -distributed.

3 OPTICAL LUMINOSITY CALCULATION

Since we have chosen to avoid using magnitude information in the calculation of the galaxy surface density distribution, we require an alternative means of deriving a normalization value for our three-dimensional luminosity profiles. To do this we have taken integrated luminosity measurements in fixed metric apertures from the literature, which allow us to infer a central luminosity density. The details of this procedure are described in Section 3.2 below.

The majority of these values are taken from the sample of Girardi et al. (2002), which incorporates most of the sample of Girardi et al. (2000). This sample comprises data from the APS and COSMOS/UKST surveys – we have selected luminosity estimates from the latter for preference, where overlaps occurred. The only exception to this is HCG 62, for which the COSMOS aperture luminosity quoted in Girardi et al. (2002) is a factor of 2 larger than the APS luminosity; for this group we have chosen the APS measurement. We note that the APS luminosity leads to a mass-to-light ratio (Section 4.2) that is more consistent with the simple estimate of Ponman & Bertram (1993). Data for three other clusters (Abell 539 and 2256, and AWM 7) were taken from Girardi et al. (2000). These latter systems have two different luminosity estimates based on literature magnitudes – we chose the ‘M(red)’ sample, since this provided the largest overall number of galaxies detected for all three clusters.

A further five systems are covered by the study of Hradecky et al. (2000), based on data from the second-generation Palomar Observatory Sky Survey (POSS II), calibrated with CCD photometry. Two groups (NGC 2563 and 5846) have luminosity estimates from Helsdon & Ponman (2003) within an aperture defined by the virial radius as calculated in Helsdon & Ponman (2000). Finally, we used the luminosity quoted in Squires et al. (1996) for the rich cluster Abell 2218. The references for each system are listed in Table 1, together with some key properties.

3.1 Conversion between bands

We have adopted the B_J photometric band as our standard reference frame, since this was used by Girardi et al. (2000, 2002), and we take $B_{\odot,J} = 5.33$ (Girardi et al. 2002). However, our other literature sources have used different bands, and so we have converted these values into the B_J band, under the assumption that the majority of the light originates in early-type galaxies. We have used the following relations to perform the conversions.

To convert from the B band to the B_J band, we assume:

$$\begin{aligned} B_{\odot} &= 5.48 \text{ (Girardi et al. 2000),} \\ B_J &= B + 0.28(B - V) \text{ (Blair \& Gilmore 1982),} \\ B - V &= 0.9, \text{ for early-type galaxies (Girardi et al. 2000),} \\ \Rightarrow B_J &= B + 0.252, \end{aligned}$$

which leads to

$$\frac{L_{B_J}}{L_{B_{\odot,J}}} = 0.691 \frac{L_B}{L_{B,\odot}}. \quad (2)$$

To convert from the V band to the B_J band, we assume:

$$\begin{aligned} V_{\odot} &= 4.82 \text{ (Allen 1973),} \\ \Rightarrow B_J &= V + 1.152, \text{ from above (for early-type galaxies),} \end{aligned}$$

which leads to

$$\frac{L_{B_J}}{L_{B_{\odot,J}}} = 0.554 \frac{L_V}{L_{V,\odot}}. \quad (3)$$

For comparison with R -band luminosities, we assume:

Table 1. Some basic properties of the 32 objects in the optical sample, listed in order of increasing temperature. Positions and redshifts are taken from Ebeling et al. (1996, 1998), Ponman et al. (1996) and NED. Columns 7–9 are data as determined in this work, except for those values of r_s marked with a \star , which were taken from Lloyd-Davies (2001). Note that values are for $H_0 = 70 \text{ km s}^{-1} \text{ Mpc}^{-1}$. All errors are 68 per cent confidence.

Name	RA (J2000)	Dec. (J2000)	z	T^a (keV)	R_{200} (arcmin)	r_s^b (arcmin)	L_{B_J} ($10^{11} L_{B_{\odot,J}}$)	M/L (M/L_{B_1}) $_{\odot}$	Reference ^c
NGC 4325	185.825	10.622	0.0252	0.90	22.4	2.6	$1.22^{+0.6}_{-0.6}$	293^{+160}_{-160}	G02 (APS)
NGC 5846	226.385	1.696	0.0058	1.18	95.5	39.3	$1.13^{+0.6}_{-0.6}$	325^{+170}_{-170}	H02
HCG 62	193.284	-9.224	0.0137	1.48	33.5	12.7 \star	$2.59^{+1.3}_{-1.3}$	78^{+40}_{-40}	G02 (APS)
NGC 5129	201.150	13.928	0.0233	1.54	20.5	7.8	$2.56^{+1.3}_{-1.3}$	82^{+48}_{-48}	G02 (APS)
NGC 2563	125.102	21.096	0.0163	1.61	31.4	12.1	$1.11^{+0.6}_{-0.6}$	256^{+130}_{-130}	H02
Abell 262	28.191	36.157	0.0163	2.03	50.4	47.0 \star	$9.71^{+4.9}_{-4.9}$	118^{+65}_{-65}	G02 (APS)
Abell 194	21.460	-1.365	0.0180	2.07	52.2	20.4	$5.16^{+2.6}_{-2.6}$	320^{+200}_{-200}	G02 (COSMOS)
MKW 4	180.990	1.888	0.0200	2.08	35.5	40.3	$1.12^{+0.6}_{-0.6}$	613^{+310}_{-310}	G02 (APS)
MKW 4S	181.647	28.180	0.0283	2.46	28.9	11.9	$3.37^{+1.2}_{-1.2}$	320^{+130}_{-130}	H00
NGC 6338	258.825	57.400	0.0282	2.64	26.4	5.9	$14.0^{+7.0}_{-7.0}$	59^{+60}_{-50}	G02 (APS)
Abell 539	79.134	6.442	0.0288	2.87	38.0	5.9	$6.17^{+3.1}_{-3.1}$	415^{+200}_{-200}	G00
AWM 4	241.238	23.946	0.0318	2.96	40.2	11.5	$4.75^{+2.4}_{-2.4}$	886^{+540}_{-540}	G02 (APS)
Abell 1060	159.169	-27.521	0.0124	3.31	104.8	15.0 \star	$18.9^{+9.5}_{-9.5}$	244^{+120}_{-120}	G02 (COSMOS)
Abell 2634	354.615	27.022	0.0309	3.45	32.1	12.0	$25.4^{+12.8}_{-12.6}$	76^{+40}_{-40}	G02 (APS)
Abell 2052	229.176	7.002	0.0353	3.45	36.6	2.3	$6.70^{+1.7}_{-1.7}$	589^{+240}_{-240}	H00
Abell 2199	247.165	39.550	0.0299	3.93	34.3	31.2 \star	$9.98^{+3.5}_{-2.4}$	211^{+60}_{-60}	H00
Abell 2063	230.757	8.580	0.0355	4.00	35.7	2.3	$7.08^{+1.7}_{-1.6}$	541^{+140}_{-140}	H00
AWM 7	43.634	41.586	0.0172	4.02	105.2	4.2 \star	$7.68^{+3.8}_{-3.8}$	1614^{+970}_{-970}	G00
Abell 3391	96.608	-53.678	0.0536	5.39	26.9	4.3	$25.1^{+12.6}_{-12.6}$	213^{+120}_{-120}	G02 (COSMOS)
Abell 2670	358.564	-10.408	0.0759	5.64	19.6	5.9	$20.7^{+10.3}_{-10.4}$	249^{+130}_{-130}	G02 (COSMOS)
Abell 119	14.054	-1.235	0.0444	6.08	33.5	5.5	$26.9^{+13.6}_{-13.4}$	218^{+120}_{-120}	G02 (COSMOS)
Abell 496	68.397	-13.246	0.0331	6.11	39.2	20.0 \star	$13.1^{+6.6}_{-6.5}$	321^{+170}_{-170}	G02 (COSMOS)
Abell 3558	201.991	-31.488	0.0477	6.28	28.7	18.2	$47.7^{+23.8}_{-23.8}$	90^{+50}_{-50}	G02 (COSMOS)
Abell 3571	206.867	-32.854	0.0397	7.31	39.8	17.9	$46.8^{+23.4}_{-23.4}$	161^{+80}_{-80}	G02 (COSMOS)
Abell 2218	248.970	66.214	0.1710	8.28	11.3	10.4 \star	$29.9^{+3.7}_{-3.8}$	266^{+60}_{-60}	S96
Abell 1795	207.218	26.598	0.0622	8.54	28.3	6.4 \star	$27.9^{+13.9}_{-14.0}$	330^{+240}_{-240}	G02 (COSMOS)
Abell 2256	256.010	78.632	0.0581	8.62	27.3	7.3	$39.2^{+19.6}_{-19.6}$	175^{+90}_{-90}	G00
Abell 85	10.453	-9.318	0.0521	8.64	28.1	11.6	$23.9^{+12.1}_{-12.0}$	229^{+120}_{-120}	G02 (COSMOS)
Abell 3266	67.856	-61.417	0.0545	9.53	29.7	12.0	$29.3^{+14.7}_{-14.7}$	261^{+140}_{-140}	G02 (COSMOS)
Abell 2029	227.729	5.720	0.0766	9.80	26.4	4.6	$86.3^{+43.0}_{-43.1}$	155^{+80}_{-80}	G02 (APS)
Abell 478	63.359	10.466	0.0882	10.95	17.8	12.8 \star	$28.1^{+7.3}_{-7.3}$	210^{+160}_{-160}	H00
Abell 2142	239.592	27.233	0.0894	11.16	22.7	8.7	$50.0^{+25.0}_{-25.0}$	250^{+170}_{-170}	G02 (APS)

Notes. ^aThe cooling flow-corrected, emission-weighted temperature of the system within $0.3R_{200}$, as determined in Paper I.

^bThe NFW scale radius of the galaxy distribution (see equation 1). ^cReferences for the luminosity data: G00 = Girardi et al. (2000); G02 = Girardi et al. (2002); H00 = Hradecky et al. (2000); H02 = Helsdon & Ponman (2003); S96 = Squires et al. (1996).

$$R_{\odot} = 4.28 \text{ (Allen 1973),}$$

$$V - R = 0.55 \text{ for early-type galaxies (Girardi et al. 2000),}$$

$$\Rightarrow B_J = R + 1.702, \text{ from above,}$$

which leads to

$$\frac{L_{B_J}}{L_{B_{\odot,J}}} = 0.547 \frac{L_R}{L_{R,\odot}}. \quad (4)$$

3.2 Determination of luminosity normalization

With the exception of the Hradecky et al. (2000) data, all our literature values of luminosity are simple estimates within a fixed aperture on the sky. As such, these measurements represent the integrated luminosity within a cylinder, defined by the aperture multiplied by the

diameter of the cluster. It was therefore necessary to allow for the projected contribution to this value from luminosity at large radii, when inferring values for the three-dimensional normalization. We accomplished this in the following way, using our numerical projection technique described previously. The normalization was set to unity and the NFW profile was integrated out to a large radius, to ensure convergence (taken to be 500 arcmin), in a series of fixed-width spherical shells. The projected emission from these shells was then computed, in the corresponding series of annuli. The total luminosity within the aperture radius was then calculated, by simply summing the contributions from the annuli within that radius. Where the aperture radius lay within an annulus, the contribution from this annulus was determined by linear interpolation, since the

annulus width is small. The appropriate normalization factor was found by dividing the measured luminosity value by that calculated for a normalization of unity.

For the five clusters analysed by Hradecky et al. (2000), a slightly different approach was taken, since the authors corrected their aperture luminosities for the effects of projection. Working in three dimensions, we set our normalization to unity and simply integrated our density profile from $r = 0$ to a radius of $1 h_{50}$ Mpc (used for all their quoted luminosities). The ratio of the aperture luminosity to the integrated value then yields the central luminosity density that we require.

The errors on our quoted luminosities are derived from the errors on the aperture values. Following Girardi et al. (2002), we assume a 1σ error of 50 per cent on our total L_{B_j} values based on their data. The same fractional error was assumed for the values from Helsdon & Ponman (2003), based on their own error estimates. The values for the Hradecky et al. (2000) data have smaller errors, as does the Squires et al. (1996) luminosity for Abell 2218, since these are based on higher-quality POSS II and CCD observations, respectively, which are more accurate than the majority of our photographic plate data.

Owing to our choice of an NFW profile for the fitting, coupled with the bias towards optically rather than X-ray selected clusters in previous studies, we are extremely restricted in the number of direct comparisons that can be made between our spatial fitting results and those available in the literature. However, we note that Adami et al. (1998) found a scale radius of 3.7 ± 0.6 arcmin for the cluster Abell 119, which is reasonably consistent with our value of 5.5 arcmin (see Table 1). This change in r_s would give a ~ 4 per cent change in the total optical luminosity within R_{200} , based on the aperture luminosity for this cluster as measured by Girardi et al. (2002). The impact of uncertainties in the spatial fitting parameters is limited by the fact that the apertures from which the optical luminosities we use for calibration have been taken are close to R_{200} : the median difference between these aperture radii and our X-ray determined values of R_{200} is ~ 50 per cent. In the case of Abell 119, our correction to the Girardi et al. (2002) aperture luminosity amounts to only ~ 10 per cent. For Abell 2256, the analysis of Oegerle et al. (1987) provides support for our findings, measuring an inner logarithmic slope of -0.98 ± 0.02 for the galaxy density distribution in this cluster. Moreover, their binned radial profile is consistent with an outer slope of -3 and a break radius similar to our value of 7.3 arcmin.

4 RESULTS: OPTICAL PROPERTIES

We convert optical light directly into stellar mass, assuming a mass-to-light ratio for early-type galaxies of $(M/L)_B = 7 h_{70}$ solar (Pizzella et al. 1997). A similar value of $(8.3 \pm 0.35) h_{70}$ was found by van der Marel (1991). Using $B_{\odot} - B_{\odot,J} = 0.15$ from Section 3.1 gives $(M/L)_{B_j} = 6.1 h_{70} (M/L_{B_j})_{\odot}$. To infer the density profile of dark matter, we subtract the gas and stellar mass from the total mass (as determined from the X-ray data). Consequently, we only have information on the dark matter and stellar properties for the optical subsample of 32 groups and clusters.

Relationships between integrated properties provide an important tool for investigating the similarity between haloes across a range of masses. Although quantities such as luminosity are directly observable, some allowance must be made for the effects of projection if fair comparisons are to be made between different systems. Correspondingly, all our quoted luminosity values (see Table 1) are derived from integrating the *three-dimensional* light profiles, using

the appropriate normalization calculated in Section 3.2, to provide a more sensitive probe of scaling properties. Where we have compared our results with those from the literature quoted in different photometric bands, we apply the correction factors given in Section 3.1 to determine equivalent values in the B_j band.

4.1 Optical luminosity

A useful test of the scaling properties of the stellar distribution is the relationship between optical luminosity and mass. Fig. 1 shows the L_{B_j} luminosity within R_{200} for the optical sample plotted against the total mass within R_{200} , as calculated in Paper I. We performed an orthogonal distance regression to fit a straight line to the data in log space, using the ODRPACK software package (Boggs et al. 1989, 1992), to take account of errors in both X and Y directions. The best-fitting relation is $\log L_{B_j} = (-1.36 \pm 1.46) + (0.93 \pm 0.10) \log M$ and the scatter in the data is 1.21 times that expected from the statistical errors alone. The logarithmic slope of this relation is flatter than, but consistent with, self-similarity (i.e. $L_{B_j} \propto M$), at the 1σ level – this reflects the slight excess in stellar density in the coolest systems referred to in Section 4.3. Performing the regression with the axes reversed leads to a scaling between light and mass of $M \propto L_{B_j}^{1.08 \pm 0.12}$.

For comparison, we have also plotted L_{B_j} against the emission-weighted temperature, as calculated in Paper I, which we show in Fig. 2. Using the same regression technique, the best-fitting relation is $\log L_{B_j} = (11.02 \pm 0.01) + (1.62 \pm 0.14) \log kT$, and the scatter in the data is 0.96 times that expected from the statistical errors alone. Furthermore, there is no evidence of any steepening in the relation or any other systematic deviation from a simple power law, indicating that this provides an accurate description of the data. The logarithmic slope of this relation is steeper than, but consistent with, self-similarity (i.e. $L_{B_j} \propto T^{1.5}$, assuming that light traces mass), at the 1σ level. However, this is due to the effect of the $M-T_X$ relation slope, which is itself significantly steeper than the self-similar relation (Paper I).

The scatter about the $L_{B_j}-T_X$ relation is rather less than that about the $M-T_X$ relation, especially considering that our mass errors are quite conservative (Paper I). This is puzzling, but may reflect the fact that the optical luminosity is dominated by the stellar contribution from the inner regions, where the gas temperature is also more heavily weighted. This would produce a tighter correlation between

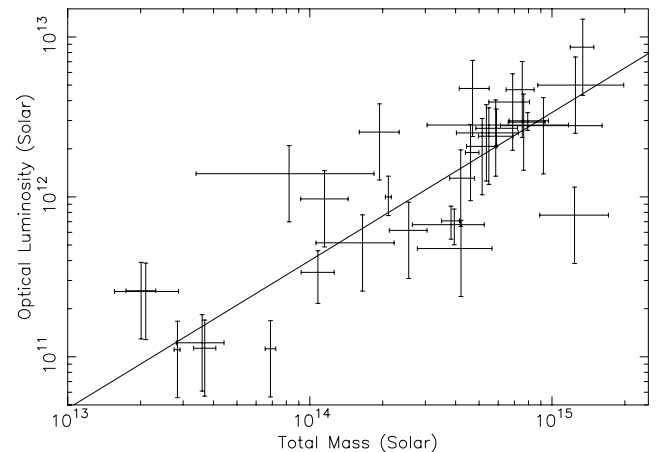


Figure 1. Total gravitating mass as a function of L_{B_j} luminosity (both within R_{200}), for the optical sample. The line shows the best-fitting power law, which has a logarithmic slope of 0.93 ± 0.10 .

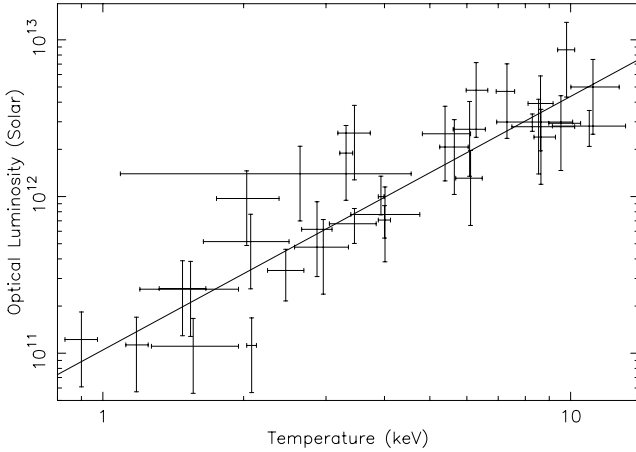


Figure 2. Total L_{B_1} luminosity within R_{200} as a function of system temperature for the optical sample. The line shows the best-fitting power law, which has a logarithmic slope of 1.62 ± 0.14 .

L_{B_1} and kT than between L_{B_1} and M , since the total mass is less sensitive to the contribution from the inner regions of the halo.

4.2 Mass-to-light ratio

Since light is easily observed, it is often used as a tracer of mass in the Universe, expressed as the ratio of total mass to optical luminosity in some photometric band. Assuming that clusters of galaxies are a fair representation of mass composition on large scales, the mass-to-light ratios in these systems can be used to estimate the total mass density of the Universe. It is therefore important to understand the scaling properties of this quantity if such cosmological inferences are to be unbiased.

Fig. 3 shows the variation in mass-to-light ratio with X-ray temperature, for the optical sample (see Table 1 for the data). It can be seen that there is little evidence of any trend in the data; Kendall's K statistic indicates the significance of a negative correlation is 0.37σ . The best-fitting power law has a logarithmic slope of -0.06 ± 0.17 , which is fully consistent with no trend. The level of scatter about

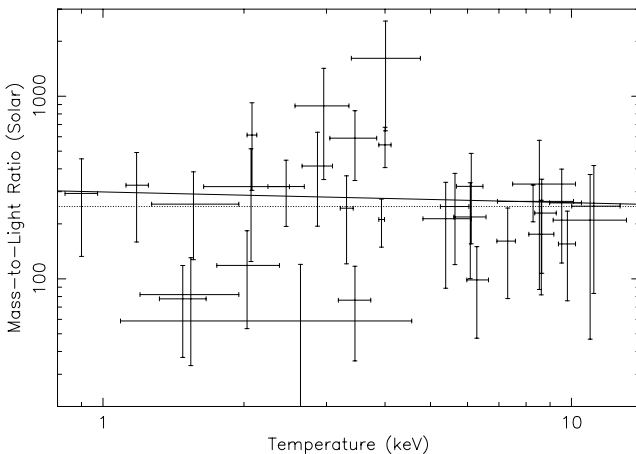


Figure 3. Mass-to-light ratio within R_{200} (in the B_1 band) as a function of system temperature for the optical sample. The solid line represents the best fitting power law, which has a logarithmic slope of -0.06 ± 0.17 . The horizontal dotted line shows the median value for the whole sample, of $249 h_{70} (M/L_{B_1})_{\odot}$.

the best fit is exactly that expected from the statistical errors. We therefore conclude that a universal mass-to-light ratio in groups and clusters provides a good description of most of our data.

It can be seen that one point in particular is very high on this relation: the poor cluster AWM 7 has $(M/L_{B_1}) \sim 1600 (M/L_{B_1})_{\odot}$, albeit with rather large errors. A large mass-to-light ratio was also measured for this system by Koranyi et al. (1998), who found a value for the R band of $(650 \pm 150) h_{100} (M/L)_{\odot}$, corresponding to $(830 \pm 190) h_{70} (M/L_{B_1})_{\odot}$, consistent with our 1σ lower bound of ~ 650 . Exclusion of this point lowers the mean of our sample from 318 ± 52 to $276 \pm 32 h_{70} (M/L_{B_1})_{\odot}$. We also note that the mass-to-light ratio for HCG 62 is rather low – only 78 ± 40 , which is rather less than the value estimated in Ponman & Bertram (1993). As was mentioned in Section 3, there is a factor of 2 difference between the aperture luminosities quoted in Girardi et al. (2002), based on APS and COSMOS data for this system. Furthermore, we note that the optically determined virial radius used for their aperture is twice as large as our X-ray measured R_{200} , which means that we have to *reduce* the Girardi et al. (2002) luminosity value, according to our fitted galaxy density profile.

To minimize the bias caused by such discrepant measurements in our M/L data, we have evaluated a *logarithmic* mean value, of $243^{+33}_{-29} h_{70} (M/L_{B_1})_{\odot}$. This is significantly lower than the ordinary, arithmetic mean value of 318 ± 52 , but compares very well with the median value of $249 h_{70} (M/L_{B_1})_{\odot}$. This illustrates the effect that anomalously large M/L systems in particular can have, when determining a representative average.

In a combined X-ray/optical study of 12 Abell clusters of galaxies, Cirimele et al. (1997) measured a mean mass-to-light ratio equivalent to $346 h_{70} (M/L_{B_1})_{\odot}$, which is consistent with our results. More recently, Hradecky et al. (2000) have also determined M/L for a sample of eight groups and clusters of galaxies, correcting their optical luminosities for projection effects, by assuming a spatial distribution of light identical to that they measured for the X-ray gas. Their mean value of M/L is equivalent to $310 \pm 45 (M/L)_{\odot}$ in the B_1 band, which is in excellent agreement with our own arithmetic mean. Furthermore, their median M/L of ~ 250 is indistinguishable from our own median value. Hradecky et al. (2000) also conclude that M/L is roughly independent of mass, as was also found by David et al. (1995), albeit based on a rather small sample in both cases. We note, however, that their assumption that the optical light traces the gas mass is not supported by our data (see Section 4.4), although this is likely to have only a small effect on their results.

The agreement with M/L as measured using optical mass estimates is generally less good, as pointed out by Hradecky et al. (2000). For example, Girardi et al. (2000) quote a mean value of $\sim 175 h_{70} (M/L_{B_1})_{\odot}$ for their sample of 105 clusters, from which many of our own luminosity estimates have been taken (since many of their results were incorporated in Girardi et al. (2002)). However, the disagreement with our own mean value of $318 \pm 52 h_{70} (M/L_{B_1})_{\odot}$ can be attributed to a difference in luminosity as well as mass: we have extended their quoted aperture L_{B_1} values, according to our fitted galaxy density profiles, and evaluated an integrated luminosity within R_{200} as derived from our X-ray data. On lower mass scales, optically derived M/L measurements are also lower than our own value. Ramella, Pisani & Geller (1997) find a mean approximately equivalent to $240 \pm 90 h_{70} (M/L_{B_1})_{\odot}$ (99 per cent confidence) for a very large sample of groups in the Northern CfA Redshift Survey, using virial mass estimates.

The difference between X-ray and optically derived masses can also be seen in the scaling properties of M/L . While our results

support a universal mass-to-light ratio in groups and clusters – consistent with the X-ray studies of Hradecky et al. (2000) and Cirimele et al. (1997) – Girardi et al. (2002) find that mass increases more quickly than luminosity, such that $M \propto L_B^{1.34 \pm 0.03}$. However, the optical study of Carlberg et al. (1996) indicates that M/L is universal in clusters, although their mean value, equivalent to $380 \pm 70 h_{70} (M/L_{B_1})_{\odot}$, is somewhat higher than our own. Weak lensing provides the most robust determination of halo mass, and the analysis of Hoekstra et al. (2001) indicated that group mass-to-light ratios were lower than those of clusters, although their sample comprised only groups. Such a variation of M/L with halo mass is confirmed by the work of Bahcall & Comerford (2002), who incorporated lensing mass estimates in part of their sample.

Semi-analytical models (SAMs) of galaxy formation generally predict a significant increase in M/L with halo mass (e.g. Kauffman et al. 1999; Benson et al. 2000; Somerville et al. 2001). As an example of the typical behaviour observed, Benson et al. (2000) find that M/L reaches a minimum on mass scales of $\sim 10^{12} M_{\odot}$, increasing by a factor of 3 up to halo masses of $10^{15} M_{\odot}$. This corresponds to a logarithmic slope of 0.16, which is only just outside the 1σ upper bound of 0.13 from our data in Fig. 3, although we only include groups and clusters in our optical sample. This tendency for M/L to increase away from a minimum on the scale of a typical galaxy is also confirmed by Marinoni & Hudson (2002). Semi-analytical models also predict that M/L in clusters is significantly lower than the global value (Kauffman et al. 1999), suggesting that even massive clusters are a biased estimator of the mean M/L in the Universe. That our findings do not provide a closer match to the M/L predictions of these models may reflect the overcooling of gas in SAMs, which is a well-known problem that leads to the formation of excessively bright central galaxies, for example (Kauffmann, White & Guiderdoni 1993).

4.3 Stellar distribution

The stellar mass density as a function of scaled radius, for the optical sample, is shown in Fig. 4, grouped into five temperature bins for clarity. There is a remarkably clear consistency in the shape and normalization of the profiles across the whole range of temperatures, which are approximately co-aligned.

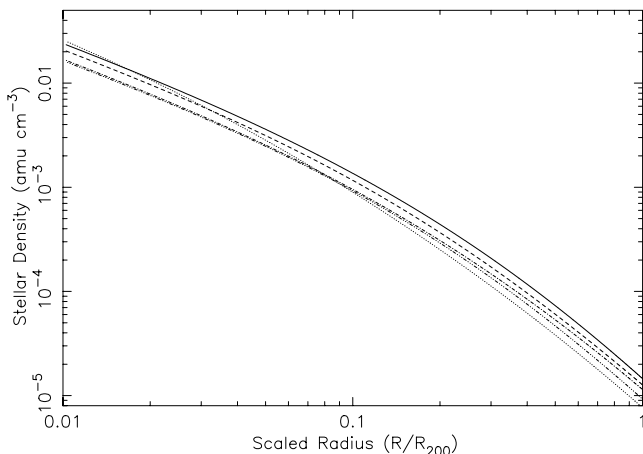


Figure 4. The variation of stellar matter density with scaled radius, for the optical sample, grouped by system temperature. The solid line represents the coolest systems (0.3–2.0 keV), increasing in temperature through dashed (2.0–2.9 keV), dotted (2.9–4.6 keV), dot-dashed (4.6–8.5 keV) and finally treble-dot-dashed (8.5–17 keV).

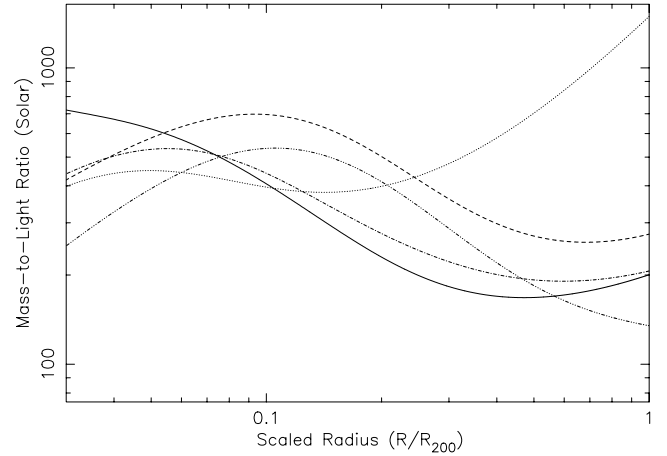


Figure 5. The variation of mass-to-light ratio (in the B_J photometric band) with scaled radius for the optical sample, grouped by system temperature. The solid line represents the coolest systems (0.3–2.0 keV), increasing in temperature through dashed (2.0–2.9 keV), dotted (2.9–4.6 keV), dot-dashed (4.6–8.5 keV) and finally treble-dot-dashed (8.5–17 keV).

Fig. 4 reveals a slight excess in the stellar density of the coolest two temperature bands, compared to the more massive systems. This points towards a possible weak trend in star formation efficiency with mass; we will revisit this issue in Section 5.5.

4.4 Spatial variation of mass-to-light ratio

The extent to which light traces mass *within* virialized haloes can be gauged by studying the mass-to-light ratio as a function of radius in these systems. Fig. 5 shows these profiles for the optical sample, grouped by temperature as before. It can be seen that there is evidence of decrease in this quantity with increasing radius, outside of $\sim 0.1 R_{200}$, in four of the five bands. Interestingly, the central range (2.9–4.6 keV) shows a clear *increase* in M/L with radius in this region, although this may be partly driven by the anomalous behaviour of AWM 7, which exhibits a strongly rising mass-to-light profile, as also found by Koranyi et al. (1998).

Outside of $\sim 0.1 R_{200}$, our results demonstrate that the distribution of optical light is more extended than that of the gravitating mass, as previously reported by David et al. (1995). It is worth noting that the simulations of Metzler & Evrard (1997) indicate that the stellar distribution can be *less* extended than that of the dark matter, as a result of the effects of dynamical friction transferring energy away from the galaxies.

We have chosen to truncate the radial scaling in Fig. 5 at $0.03 R_{200}$, rather than $0.01 R_{200}$, as our optical luminosities are likely to be unreliable in the core of the halo. This is because our unweighted galaxy density fitting is insensitive to the excess luminosity associated with a central cD galaxy. However, we would therefore expect to *underestimate* the luminosity in the core, which would overestimate the mass-to-light ratio and hence flatten any drop in M/L in the centre. This suggests that the observed trend towards a decrease in the mass-to-light ratio $\lesssim 0.1 R_{200}$ is probably real. We also note that a similar decline in M/L towards the centre is seen in the central regions of most of the 12 clusters in the sample of Cirimele et al. (1997). A recent detailed *Chandra* analysis of Abell 2029 also reveals a sharp decrease in M/L within $0.1 R_{200}$ (Lewis, Buote & Stocke 2003).

5 RESULTS: DARK MATTER, GAS AND TOTAL MASS PROPERTIES

Building on our analysis of the optical properties of our subsample of 32 groups and clusters, we now present equivalent information for the other mass components. Since we infer the dark matter distribution using our knowledge of the stellar mass profile, we are limited to our ‘optical subsample’ in the analysis of its properties. However, the gas and total gravitating mass are determined from the X-ray data alone, and so here we are able to improve our statistics by using data from the full sample, rather than being limited to those systems for which we have optical data.

5.1 Dark matter distribution

The spatial variation of the density of dark matter can be seen in Fig. 6, for the optical sample. The similarity between the hottest four temperature bands is quite close, with only the coolest systems showing a deviation from the general trend, and then only within $\sim 0.1 R_{200}$. The dark matter distribution is largely self-similar, as a consequence of its insensitivity to the types of heating and/or cooling processes that can influence baryonic material. Despite this, it is clear that there is evidence of an enhanced central density in the core of the average density profiles of the coolest groups. We return to this unusual behaviour in more detail in Section 5.4.

5.2 Total density

To provide some comparison with the density profiles of the separate mass components, we have plotted the profiles of integrated overdensity in Fig. 7, i.e. the mean density within a given radius, normalized to the critical density of the Universe. Since the gravitating mass profile is determined from the X-ray data, Fig. 7 incorporates our whole sample, including the two early-type galaxies. Correspondingly, we have a much better coverage of the low-mass end of the sample, and so have used a narrower temperature range for the coolest band (0.3–1.3 keV, instead of 0.3–2.0 keV) to provide greater sensitivity to any possible enhancements in density concentration at this mass scale.

The dark matter accounts for the majority of the gravitating mass, so it is not surprising that the trend seen in Fig. 6 is present in Fig. 7.

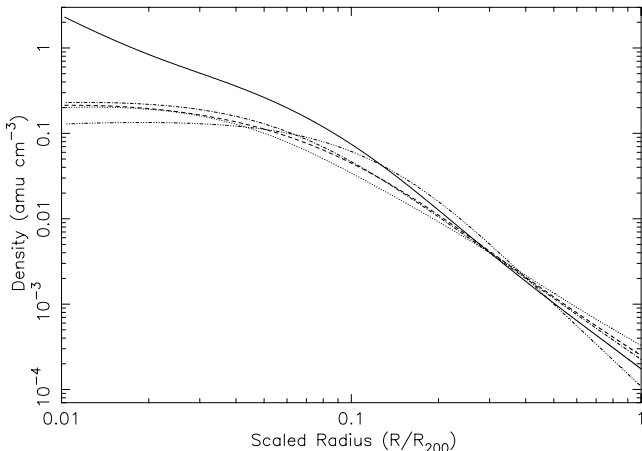


Figure 6. The variation of dark matter density with scaled radius, for the optical sample, grouped by system temperature. The solid line represents the coolest systems (0.3–2.0 keV), increasing in temperature through dashed (2.0–2.9 keV), dotted (2.9–4.6 keV), dot-dashed (4.6–8.5 keV) and finally treble-dot-dashed (8.5–17 keV).

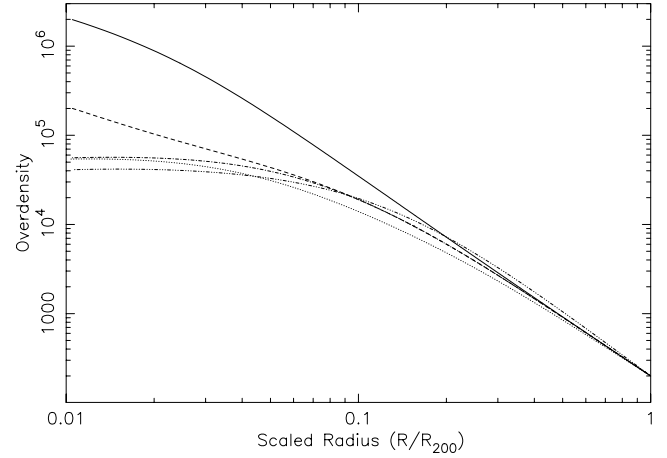


Figure 7. Spatial variation of cumulative total density – normalized to the critical density of the Universe – with scaled radius, for the full sample, grouped by system temperature. The solid line represents the coolest systems (including the two galaxies) (0.3–1.3 keV), increasing in temperature through dashed (1.3–2.9 keV), dotted (2.9–4.6 keV), dot-dashed (4.6–8 keV) and finally treble-dot-dashed (8–17 keV).

The difference between the dark matter and total mass density seen in the second coolest bin can be attributed to the slightly different temperature ranges in each case, used for reasons explained previously.

Although the total density profiles in Fig. 7 are essentially self-similar in the outer regions, there is still a reasonable degree of scatter. We have compared R_{200} with two different radii of overdensity, for each object in our X-ray sample: we have selected R_{2500} and R_{500} , which are often used in the literature (e.g. Allen, Schmidt & Fabian 2001; Finoguenov, Reiprich & Böhringer 2001b), since X-ray haloes are more readily traceable out to these radii than to R_{200} . We find that, on average, an overdensity of 2500 and 500 correspond to 31 and 66 per cent of R_{200} , respectively, with corresponding standard deviations across our sample of 5 and 4 per cent.

5.3 Gas distribution

Fig. 8 shows the gas density profiles for the whole X-ray sample, averaged according to their mean X-ray temperature. It is very clear that there is a great deal of variation in the five different curves. Even for the three profiles representing clusters hotter than 2.9 keV, there is a variation in the normalization of the lines, although the shapes of the profiles are very similar.

The two coolest temperature bands exhibit very different behaviour, having the lowest gas density within $0.3 R_{200}$ and showing no evidence of the central core seen in the hotter clusters. The normalization of the cool group lines is consistent with the trend towards a lowering of gas density compared to the clusters. This behaviour mirrors the trend seen in the gas fraction in Paper I, and provides strong evidence of a deviation from self-similar scaling of the IGM both within as well as between haloes of different masses.

5.4 Central density concentration

Although the underlying gravitational potential in virialized systems is expected to be self-similar, simulations indicate that the concentration of the dark matter should vary slightly with mass (Navarro

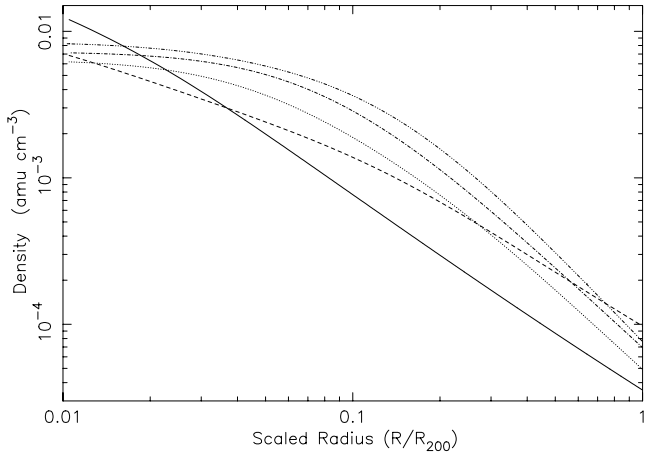


Figure 8. The variation of gas density with scaled radius, for the full sample, grouped by system temperature. The solid line represents the coolest systems (including the two galaxies) (0.3–1.3 keV), increasing in temperature through dashed (1.3–2.9 keV), dotted (2.9–4.6 keV), dot-dashed (4.6–8 keV) and finally treble-dot-dashed (8–17 keV).

et al. 1997). It was shown in Figs 6 and 7 that the coolest systems in our sample do indeed appear to be more centrally concentrated – an effect that is most pronounced in the central ~ 10 per cent of R_{200} .

To understand what is driving this behaviour, we have examined the scaling properties of the constant density core in the gas distribution, r_c , as measured from the X-ray data in Paper I. The left-hand panel of Fig. 9 shows r_c as a fraction of R_{200} plotted against system temperature. For the hottest clusters the points scatter about a self-similar mean value of roughly 10 per cent. As the temperature decreases, however, the scatter increases and $\lesssim 1$ keV there is a very sharp drop. This trend is in excellent agreement with the predictions of the galaxy formation-regulated gas evolution model of Bryan (2000), as studied in detail by Wu & Xue (2002): there is a remarkable similarity between Fig. 9 and the model and data points in fig. 8 from the latter paper.

To minimize the possibility of systematic bias in this result, we have identified and excluded from Fig. 9 those systems for which the core radius may be unreliable, as a result of the presence of a central cooling emission excess. In 17 cases, r_c was measured to be *smaller* than the size of either the radius used to excise the cooling flow

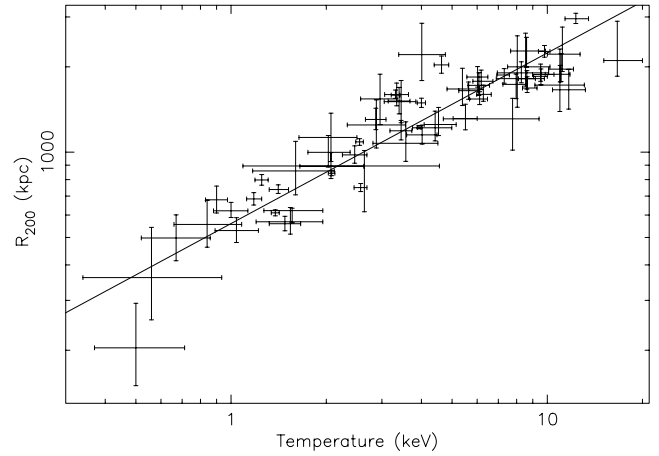
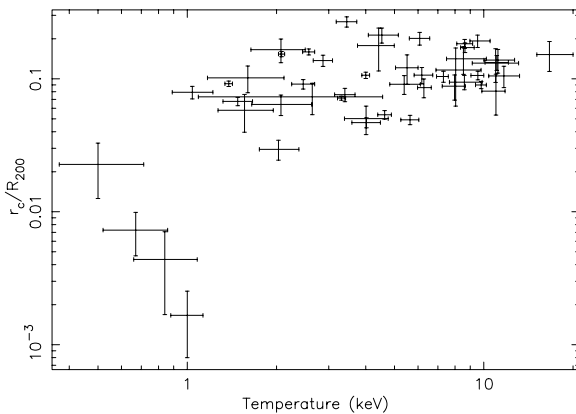


Figure 10. The variation of R_{200} as a function of temperature. The solid line depicts the best-fitting linear relation, with a slope of 0.60 ± 0.03 .

or the radius within which a cooling flow component was fitted. In addition, the cluster Abell 2218 was excluded, since it was necessary to fix its core radius at the best-fitting value in order to stabilize the fitting during the calculation of parameter errors (Paper I), leaving a total of 48 systems plotted in Fig. 9. To suppress the scatter in the relation, we have grouped the points together to a minimum of four points per bin, giving a total of 12 bins. The errors on each point are determined from the scatter in the X and Y directions. This plot is shown in the right-hand panel of Fig. 9. The underlying trend in the data is much clearer – it can be seen that the coolest bin is at least 10σ lower than the flat relation established by the six hottest bins.

It is difficult to explain this behaviour in terms of a fitting bias. Had these coolest systems exhibited X-ray core radii consistent with the cluster trend, i.e. $\gtrsim 3$ times larger than observed, they would very easily have been detected. One possibility is that the values of R_{200} are anomalously large. To test this we have plotted R_{200} against temperature in Fig. 10. The slope of this relation is somewhat steeper than the self-similar prediction of 0.5, but there is clearly no evidence of a trend towards an unusually large R_{200} in the cooler systems, which could account for the discontinuity observed in r_c/R_{200} . The most clearly discrepant point at the low-mass end is the S0 galaxy NGC 1553 (the coolest system in our sample), but it appears to have a value of R_{200} , which is *lower* than its temperature would

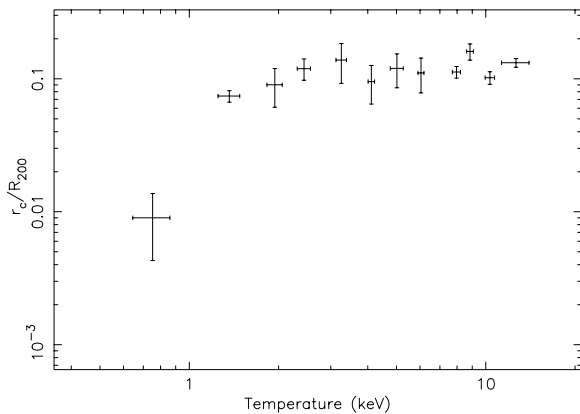


Figure 9. The ratio of r_c to R_{200} as a function of temperature. The left-hand panel shows all the individual points; the right-hand panel shows the data grouped to a minimum of four points per bin. The axes in each plot have been scaled identically. The 18 systems with potentially unreliable core radii have been excluded (see text for details).

suggest. However, this object has unusual properties, which point to an anomalously high temperature, which may have been boosted by energy injection from stellar winds (see Paper I).

5.5 Star formation efficiency and gas loss from haloes

To address the issue of star formation efficiency, we have examined the star-to-baryon ratio as a measure of the effectiveness with which gas has been converted into stellar material. The upper left-hand panel of Fig. 11 shows this quantity plotted against system temperature for the optical sample. It can be seen that there is some evidence of a negative correlation, which is significant at the 3.1σ level. However, this trend is potentially misleading, since it may be due at least in part to the variation in gas mass with temperature seen above. This means that some allowance must be made for the possibility that gas may be lost to the system beyond the virial radius, i.e. the gas mass may be reduced without any corresponding increase in the stellar mass.

A better discriminator of star formation efficiency is obtained if the stellar mass is normalized to the mass of dark matter, since this component is largely immune to bias from non-gravitational processes. We have plotted this ratio against X-ray temperature in the upper right-hand panel of Fig. 11. It is clear that the trend seen in the upper left-hand panel of Fig. 11 has largely vanished, leaving only

0.8σ evidence for a systematic variation in star formation efficiency with halo temperature.

To identify the cause of the trend in the top left-hand panel of Fig. 11, we have also plotted the ratio of gas to dark matter mass, shown in the lower left-hand panel of Fig. 11. A positive correlation between this ratio and the X-ray temperature is significant at the 3.3σ level. This confirms that the variation in gas fraction with temperature does indeed fully account for the trend found in the stellar-to-baryon ratio.

5.6 Baryon fraction and constraints on Ω_m

Using our measured stellar and gas mass data, we are able to determine the fraction of mass in baryons, f_b , for our optical sample, which we show plotted against X-ray temperature in the lower right-hand panel of Fig. 11. There is evidence of a modest trend in the data (2.5σ significance, using Kendall's K statistic – a non-parametric correlation test). The best-fitting power law is represented by the solid line, and is given by $\log f_b = (0.37 \pm 0.15)\log kT - (0.99 \pm 0.10)$; the median value of 0.161 is indicated by the horizontal dotted line.

If virialized systems constitute a fair sample of the baryon content of the Universe, we can use this median value to constrain the total mass density, $\Omega_m = \Omega_b/f_b$. Assuming a baryon density of $\Omega_b = 0.044 \pm 0.004 h_{70}^{-2}$, from measurements of the power spectrum of

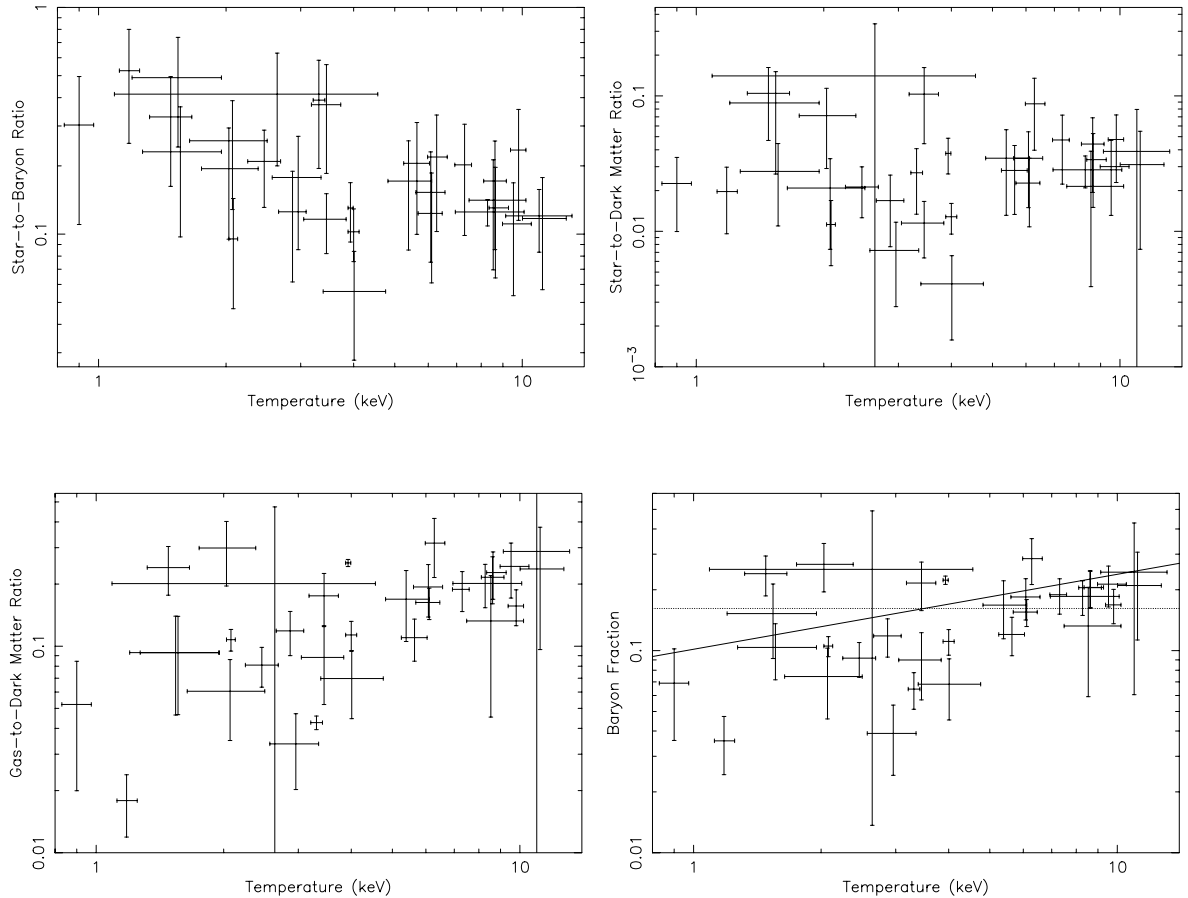


Figure 11. Top left-hand panel: the fraction of baryons in the form of stars, within R_{200} , as a function of system temperature, for the optical sample. Top right-hand panel: the ratio of stellar to dark matter mass within R_{200} , as a function of system temperature, for the optical sample. Bottom left-hand panel: the ratio of gas to dark matter mass within R_{200} , as a function of system temperature, for the optical sample. Bottom right-hand panel: baryon fraction within R_{200} as a function of system temperature, for the optical sample. The solid line represents the best-fitting power law, which has a logarithmic slope of 0.37 ± 0.15 . The dotted line marks the median value of 0.161.

the cosmic microwave background, using *WMAP* (Bennett et al. 2003), we infer a value of $\Omega_m = 0.27 h_{70}^{-1}$. This agrees well with the results of Hradecky et al. (2000).

If we improve our statistics by combining our mean stellar fraction, of (0.034 ± 0.006) , with our mean gas fraction for the full X-ray sample (Paper I), of $(0.134 \pm 0.01) h_{70}^{-3/2}$, f_b increases to 0.168 and Ω_m drops to 0.26. Assuming an unbiased measurement of the stellar and gas fraction, this represents an upper limit on Ω_m , since any baryonic component to the dark matter would increase f_b . Both these values are in good agreement with the latest measurements of $\Omega_m = 0.27 \pm 0.04$ from *WMAP* (Bennett et al. 2003).

This limit on Ω_m is slightly lower than the value of $0.30^{+0.04}_{-0.03}$ inferred by Allen et al. (2002), based on a *Chandra* analysis of six massive lensing clusters. The discrepancy arises partly from a difference in gas fraction and partly from Allen et al.'s choice of stellar to gas ratio. They use a value of $0.19 h^{0.5}$ for the latter quantity (Fukugita, Hogan & Peebles 1998; White et al. 1993), which is rather less than our measured value of 0.30 ± 0.04 . However, the latter value of 0.30 is heavily biased by a handful of groups, which have a particularly high fraction of stellar baryons (the uppermost points in the top left-hand panel of Fig. 11); the median stellar to gas ratio for our sample is 0.21, in much better agreement with existing measurements, which are based on more massive clusters.

Moreover, the Allen et al. (2002) mean measured gas fraction is 0.113 ± 0.005 , compared to our mean of 0.134 ± 0.01 for the whole X-ray sample (Paper I). The cause of the discrepancy in both cases is the scaling behaviour of the gas fraction – we find evidence of a rise in gas fraction with radius, whereas Allen et al. report a substantially flat f_{gas} profile in a number of their clusters, albeit restricted to a radius of overdensity of R_{2500} . By extrapolating a constant value out to R_{200} , no allowance is made for an increase in f_{gas} , as is predicted by numerical simulations, even when the effects of preheating and radiative cooling are absent (Eke et al. 1998; Frenk et al. 1999).

Furthermore, we find evidence of a decrease in f_{gas} in cooler systems, which has the effect of lowering our mean value. Given the possible impact of non-gravitational heating on low-mass systems, the gas fraction in richer clusters is likely to be a better indicator of the universal value. If we calculate an average gas fraction for our hottest clusters (>5 keV), we obtain an even higher value, of 0.17 ± 0.01 . Combined with our mean stellar fraction from above, this places a more stringent upper limit on the mass density, of $\Omega_m \leq 0.22 h_{70}^{-1}$, which lies just below the *WMAP* 1σ confidence interval.

6 DISCUSSION

6.1 Implications for heating/cooling

Our results confirm the systematic breaking of self-similarity in the IGM that was observed in the gas fraction in Paper I. Clearly the thermal history of the hot gas has been altered by the influence of non-gravitational physics. The most promising candidates are radiative cooling (Bryan 2000; Muanwong et al. 2001) and energy injection by heating (e.g. Valageas & Silk 1999). Both mechanisms are able to account for the X-ray observations: more efficient cooling in denser (smaller) haloes leads to a depletion of gas in the inner regions; the energetically boosted IGM is only weakly captured in the shallower potential wells of less massive virialized systems, thus reducing their gas fraction.

The apparent self-similarity of the stellar distribution with respect to the dark matter suggests that star formation has similar efficiency in both groups and clusters. However, the behaviour of the gas to dark matter ratio points to gas loss in the cooler systems, albeit

subject to significant extrapolation of the data. Together, these results are more suggestive of non-gravitational heating as the likely mechanism responsible for the observed breaking of self-similarity in virialized systems, since this would more naturally account for depletion of gas in cooler systems without a corresponding enhanced stellar mass. The alternative, radiative cooling, would only be able to reduce gas mass by associated star formation, unless it is able to form baryonic dark matter – for example, molecular clouds (e.g. Pfenniger, Combes & Martinet 1994).

The cooling hypothesis (cf. Knight & Ponman 1997) has received increased attention lately, particularly in relation to the observed entropy properties of virialized systems – indeed our own results (see Ponman, Sanderson & Finoguenov 2003, Paper III) are consistent with some of the predictions of such models, when the effects of feedback from associated star formation are allowed for (Voit & Bryan 2001). However, the natural consequence of increased gas cooling is enhanced star formation, unless a substantial reservoir of baryons exists in the form of less luminous matter – e.g. molecular clouds (Edge 2001). The stellar properties of our sample of virialized systems appear consistent with the predictions of self-similar scaling, and we find no evidence for a significant variation in star formation efficiency across a wide range of halo masses. Therefore, we conclude that heating must have had at least some role to play in systematically modifying the properties of the IGM.

6.2 Halo formation epoch

From both the dark matter and total mass density profiles, it is clear that there is an enhancement in the central concentration in the very coolest systems in our sample. This behaviour is consistent with hierarchical structure formation (e.g. Blumenthal et al. 1984), in which the smallest haloes collapse at the earliest epochs: the higher density of the Universe at this time results in a higher central density. Such a systematic variation in the epoch of formation of virialized systems has previously been observed (Sato et al. 2000).

Another possibility is that the greater ages for these systems allow more time for accumulation of extra material on to their haloes, via accretion (Salvador-Solé et al. 1998). This process would have the effect of increasing the virial radius, but without significantly modifying the characteristic turnover radius in the gas density profile, i.e. the X-ray core radius as a fraction of R_{200} would shrink, as observed in Section 5.4. Although small haloes are still able to form at the present epoch, there may be an intrinsic bias towards observing older, more relaxed systems, which are likely to be brighter – indeed, we selected our X-ray sample principally on the basis of a regular X-ray morphology. Thus we might expect to find fewer examples of cool systems with large a core, compared to their virial radius. This may account for the absence of points around the cluster trend of $r_c/R_{200} \approx 0.1$ below ~ 1 keV in Fig. 9.

The formation epoch of virialized haloes may play quite a significant role in influencing their scaling properties. This is particular true for nearby systems, where the redshift of observation, z_{obs} , is a poor and systematically biased estimator of the redshift of formation, z_f . The trend for less massive haloes to be older may account for the observed steepening of the $M-T_X$ relation (see Paper I), in contrast to the apparently self-similar slope found in more distant, massive clusters (Allen et al. 2001), where z_{obs} is a much better measure of z_f . However, the simulations of Mathiesen (2001) indicate that this process has a negligible effect on the temperatures of those clusters which have assembled 75 per cent of their final mass by $z = 0.6$.

7 CONCLUSIONS

We have conducted a detailed study of the mass composition of a large sample of virialized systems. Using X-ray data for our whole sample of 66 objects, we have derived the gas and total gravitating mass profiles as a function of radius. Optical data for a subsample of 32 groups and clusters have allowed us to determine the stellar mass distribution, and thus infer the dark matter density profile.

We have determined the deprojected luminosity distribution from unweighted surface density fits to galaxy positions from the APM survey, combined with aperture luminosity measurements taken from a small number of sources in the literature. Using the galaxy density profile we are able to extrapolate the light to our nominal virial radius of R_{200} (as determined from the X-ray data) to yield the *deprojected* optical luminosity, in the B_J photometric band.

The scaling properties of the total B -band optical luminosity within R_{200} are consistent with self-similarity: $M \propto L^{1.08 \pm 0.12}$ and $L \propto T^{1.62 \pm 0.14}$, for total mass and emission-weighted temperature, respectively. Similarly, the mass-to-light ratio remains essentially constant across the sample, showing no trend with X-ray temperature ($M/L \propto T^{-0.06 \pm 0.17}$); we find a logarithmic mean M/L of $243^{+33}_{-29} h_{70} (M/L_{B_J})_{\odot}$, in good agreement with other measurements based on X-ray mass estimates. Our data therefore provide no evidence for a significant increase in star formation rate in galaxy groups, which is constant across most of the sample.

We find that the dark matter is the most centrally concentrated mass component, followed by the galaxies, with the X-ray emitting IGM the most extended component. Comparing the spatial distribution of these mass components across two decades of halo mass, we find that the dark matter and total mass density profiles of our sample are nearly self-similar, but for a clear central excess in the coolest systems ($\lesssim 1.5$ keV). We attribute this enhancement in central density concentration to a sharp decline in the size of the gas core radius r_c (normalized to R_{200}) amongst systems cooler than ~ 1 keV. Surprisingly, we find that there is very little variation in the shape and normalization of the stellar density profile across the sample. However, the gas density clearly departs from this trend: the IGM is significantly more extended and less dense in smaller haloes.

We measure a mean stellar mass fraction of (0.032 ± 0.004) and a median baryon fraction, for our optical sample, of $0.161 h_{70}^{-3/2}$. This allows us to place an upper limit of the mass density of the Universe of $\Omega_m \leq 0.27 h_{70}^{-1}$, though it is possible that somewhat lower values are indicated by our data: if we restrict our analysis to clusters hotter than 5 keV we deduce $\Omega_m \leq 0.22 h_{70}^{-1}$. This change is a consequence of a trend in f_{gas} with temperature, resulting from the influence of non-gravitational processes on the intracluster gas. Our results favour energy injection by non-gravitational heating as a contributory mechanism for explaining the observed breaking of self-similarity in the IGM, since radiative cooling alone would lead to a significant increase in star formation efficiency in groups, in contrast to our findings.

As improved X-ray mass estimates are obtained, with *XMM-Newton* and *Chandra*, and the technology of wide-field optical CCD photometry continues to advance, the prospects for very accurate determination of the mass-to-light ratio and baryon content in virialized systems look good.

ACKNOWLEDGMENTS

We are grateful to Alexis Finoguenov, Ed Lloyd-Davies and Maxim Markevitch for providing the X-ray data and contributing to the orig-

inal analysis. AJRS thanks Alastair Edge and Somak Raychaudhury for helpful comments and suggestions and Yen-Ting Lin for useful discussions. We are grateful to the referee for suggesting several improvements to the paper. AJRS acknowledges financial support from the University of Birmingham. This work has made use of the Starlink facilities at Birmingham, the Automatic Plate Measuring (APM) machine catalogue at Cambridge and the NASA/IPAC Extragalactic Database (NED).

REFERENCES

- Adami C., Katgert P., Biviano A., 1998, *A&A*, 336, 63
 Allen C. W., 1973, *Astrophysical Quantities*, 3rd edn. Athlone Press, London
 Allen S. W., Schmidt R. W., Fabian A. C., 2001, *MNRAS*, 328, L37
 Allen S. W., Schmidt R. W., Fabian A. C., 2002, *MNRAS*, 334, L11
 Avila-Reese V., Firmani C., Klypin A., Kravtsov A. V., 1999, *MNRAS*, 310, 527
 Bahcall N. A., Comerford J. M., 2002, *ApJ*, 565, L5
 Beers T. C., Tonry J. L., 1986, *ApJ*, 300, 557
 Bennett C. L. et al., 2003, *ApJs*, 148, 1
 Benson A. J., Cole S., Frenk C. S., Baugh C. M., Lacey C. G., 2000, *MNRAS*, 311, 793
 Blair M., Gilmore G., 1982, *PASP*, 94, 742
 Blumenthal G. R., Faber S. M., Primack J. R., Rees M. J., 1984, *Nat*, 311, 517
 Boggs P. T., Byrd R. H., Donaldson J. R., Schnabel R. B., 1989, *ACM Trans. Math. Software*, 15(4), 348
 Boggs P. T., Byrd R. H., Rogers J. E., Schnabel R. B., 1992, *User's Reference Guide for ODRPACK Version 2.01*
 Bryan G. L., 2000, *ApJ*, 544, L1
 Caretta C. A., Maia M. A. G., Willmer C. N. A., 2000, *AJ*, 119, 524
 Carlberg R. G., Yee H. K. C., Ellingson E., Abraham R., Gravel P., Morris S., Pritchet C. J., 1996, *ApJ*, 462, 32
 Carlberg R. G., Yee H. K. C., Ellingson E., 1997, *ApJ*, 478, 462
 Castillo-Morales A., Schindler S., 2003, *A&A*, 403, 433
 Cirimele G., Nesci R., Trévese D., 1997, *ApJ*, 475, 11
 Davé R., Katz N., Weinberg D. H., 2002, *ApJ*, 579, 23
 David L. P., Jones C., Forman W., 1995, *ApJ*, 445, 578
 Ebeling H., Voges W., Böhringer H., Edge A. C., Huchra J. P., Briel U. G., 1996, *MNRAS*, 281, 799
 Ebeling H., Edge A. C., Böhringer H., Allen S. W., Crawford C. S., Fabian A. C., Voges W., Huchra J. P., 1998, *MNRAS*, 301, 881
 Edge A. C., 2001, *MNRAS*, 328, 762
 Eke V. R., Navarro J. F., Frenk C. S., 1998, *ApJ*, 503, 569
 Fabricant D. G., Kent S. M., Kurtz M. J., 1989, *ApJ*, 336, 77
 Finoguenov A., Arnaud M., David L. P., 2001a, *ApJ*, 555, 191
 Finoguenov A., Reiprich T. H., Böhringer H., 2001b, *A&A*, 368, 749
 Frenk C. S. et al., 1999, *ApJ*, 525, 554
 Fukugita M., Hogan C. J., Peebles P. J. E., 1998, *ApJ*, 503, 518
 Girardi M., Biviano A., Giuricin G., Mardirossian F., Mezzetti M., 1995, *ApJ*, 438, 527
 Girardi M., Borgani S., Giuricin G., Mardirossian F., Mezzetti M., 2000, *ApJ*, 530, 62
 Girardi M., Manzato P., Mezzetti M., Giuricin G., Limboz F., 2002, *ApJ*, 569, 720
 Helsdon S. F., Ponman T. J., 2000, *MNRAS*, 315, 356
 Helsdon S. F., Ponman T. J., 2003, *MNRAS*, 340, 485
 Hoekstra H. et al., 2001, *ApJ*, 548, L5
 Hradecky V., Jones C., Donnelly R. H., Djorgovski S. G., Gal R. R., Odewahn S. C., 2000, *ApJ*, 543, 521
 James F., 1998, *CERN Program Library Long Writeup D506*
 Jing Y. P., 2000, *ApJ*, 535, 30
 Kauffmann G., White S. D. M., Guiderdoni B., 1993, *MNRAS*, 264, 201
 Kauffman G., Colberg J. M., Diaferio A., White S. D. M., 1999, *MNRAS*, 303, 188
 Knight P. A., Ponman T. J., 1997, *MNRAS*, 289, 955
 Koranyi D. M., Geller M. J., 2000, *AJ*, 119, 44

- Koranyi D. M., Geller M. J., 2002, *AJ*, 123, 100
Koranyi D. M., Geller M. J., Mohr J. J., Wegner G., 1998, *AJ*, 116, 2108
Lewis A. D., Buote D. A., Stocke J. T., 2003, *ApJ*, 586, 135
Lloyd-Davies E. J., 2001, PhD thesis, Univ. Birmingham, UK
Marinoni C., Hudson M. J., 2002, *ApJ*, 569, 101
Mathiesen B. F., 2001, *MNRAS*, 326, L1
Merritt D., Tremblay B., 1994, *AJ*, 108, 514
Metzler C. A., Evrard A. E., 1997, preprint (astro-ph/9710324)
Mohr J. J., Geller M. J., Fabricant D. G., Wegner G., Thorstensen J., Richstone D. O., 1996, *ApJ*, 470, 724
Muanwong O., Thomas P. A., Kay S. T., Pearce F. R., Couchman H. M. P., 2001, *ApJ*, 552, L27
Navarro J. F., Frenk C. S., White S. D. M., 1995, *MNRAS*, 275, 720
Navarro J. F., Frenk C. S., White S. D. M., 1997, *ApJ*, 490, 493
Oegerle W. R., Jewison M. S., Hoessel J. G., 1987, *AJ*, 93, 519
Pfenniger D., Combes F., Martinet L., 1994, *A&A*, 285, 79
Pizzella A. et al., 1997, *A&A*, 323, 349
Ponman T. J., Bertram D., 1993, *Nat*, 363, L51
Ponman T. J., Bourner P. D. J., Ebeling H., Böhringer H., 1996, *MNRAS*, 283, 690
Ponman T. J., Sanderson A. J. R., Finoguenov A., 2003, *MNRAS*, 343, 331 (Paper III)
- Pratt G. W., Arnaud M., 2002, *A&A*, 394, 375
Ramella M., Pisani A., Geller M. J., 1997, *AJ*, 113, 483
Rines K., Geller M. J., Diaferio A., Mahdavi A., Mohr J. J., Wegner G., 2002, *AJ*, 124, 1266
Salvador-Solé E., Solanes J. M., Manrique A., 1998, *ApJ*, 499, 542
Sanderson A. J. R., Ponman T. J., Finoguenov A., Lloyd-Davies E. J., Markevitch M., 2003, *MNRAS*, 340, 989 (Paper I)
Sarazin C. L., 1980, *ApJ*, 236, 75
Sato S., Akimoto F., Furuzawa A., Tawara Y., Watanabe M., Kumai Y., 2000, *ApJ*, 537, L73
Somerville R. S., Lemson G., Sigad Y., Dekel A., Kauffmann G., White S. D. M., 2001, *MNRAS*, 320, 289
Squires G., Kaiser N., Babul A., Fahlman G., Woods D., Neumann D. M., Böhringer H., 1996, *ApJ*, 461, 572
Valageas P., Silk J., 1999, *A&A*, 347, 1
van der Marel R. P., 1991, *MNRAS*, 253, 710
Voit G. M., Bryan G. L., 2001, *Nat*, 414, 425
White D. A., Navarro J. F., Evrard A. E., Frenk C. S., 1993, *Nat*, 366, 429
Wu X., Xue Y., 2002, *ApJ*, 569, 112

This paper has been typeset from a $\text{\TeX}/\text{\LaTeX}$ file prepared by the author.